CrystEngComm

ROYAL SOCIETY OF CHEMISTRY

COMMUNICATION

View Article Online
View Journal

Check for updates

Cite this: DOI: 10.1039/d6ce00207b

Received 13th March 2026,
Accepted 21st May 2026

DOI: 10.1039/d6ce00207b

rsc.li/crystengcomm

Role of liquid water distribution in MgO hydroxylation

Vitalii Starchenko, *[a] Sai Adapa, [a] Lawrence M. Anovitz, [a] Ilia Ivanov, [b] Andrew G. Stack, [a] Ke Yuan [a] and Juliane Weber [a]

We demonstrate how the spatial distribution of water on the MgO single crystal surfaces controls the texture of a new phase, $Mg(OH)_2$, formed during a dissolution–precipitation reaction. Modeled liquid–vapor phase separation near the solid–liquid interface demonstrates the formation of a homogeneous film as opposed to isolated droplets depending on the surface wettability properties. Modeling results confirm that our experimental observation of droplet-like features during formation of $Mg(OH)_2$ on the MgO surface is driven by the temperature-dependent interfacial properties.

Hydroxylation and oxidation of inorganic films and mineral surfaces in an environment containing water vapor is important for a variety of applications including performance of microelectronic devices,[1–3] quantum materials stability,[4–6] and CO_2 removal *via* direct air capture.[7–9] Magnesium oxide is widely used for various thin film applications,[10–13] as a sorbent material for CO_2 capture reactions,[14–16] and as a high-temperature optical material. Recent analyses of the reactivity of MgO exposed to water have shown a structured water monolayer at the MgO(100) surface,[17] a multistep reaction pathway to form hydroxides,[18] and MgO passivation in humid CO_2 environments.[14] The commonly accepted reaction pathway for MgO exposed to water includes four steps: hydroxylation, adsorption, dissolution, and precipitation.[18] However, multiple studies at the meso- and macro-scales report that the morphologies of the $Mg(OH)_2$ precipitate take multiple forms which can't be explained by the reaction rates alone.[19–21] Moreover, several experimental studies on reactivity with CO_2 reported on the essential role of humidity,[22–24] indicating that the most efficient carbonation occurs at a relative humidity of over 80%.

Therefore, one can hypothesize that MgO mineral reactivity depends, in part, on the distribution of water on the surface. In most studies a uniform distribution of water down to several water molecules is assumed.[25–27] However, the balance between the interfacial free energies as described by the Young–Laplace equation suggests that under some conditions surface tension prevents the liquid droplet from spreading infinitely across the solid surface.

It has been demonstrated that liquid–vapor systems can be effectively studied using a phase-field approach with a classical double well potential expression for the thermodynamic free energy.[28] Moreover, the van der Waals theory of capillarity allows one to model realistic systems in which the free energy can be expressed in terms of the fluid density based on the equation of state.[29,30]

In this study we investigated (i) the effect of different substrate wettability properties on interfacial liquid–vapor density distributions and (ii) the effect of temperature on this density distribution. We utilize the phase field modeling approach to explain experimental observations qualitatively. Our results demonstrate that the transition from a uniform film to isolated water droplets/islands is controlled by the surface wettability, and increased temperature amplifies this effect. This is confirmed by comparison of the simulation results with experimental observations.[31] This analysis indicates that this phenomenon plays a key role in controlling water distributions at the interface, which change the final texture and distribution of the $Mg(OH)_2$ precipitate.

The MgO crystals used in our experiments were grown using the carbon-arc fusion technique at Oak Ridge National Laboratory.[32] These MgO crystals were synthesized 27 years before current experiments, and stored at ambient conditions exposed to air. Prior to experiments, MgO crystals were cleaved along (100) crystallographic plane into blocks approximately 3 mm in size and cleaned by sonication in isopropanol for 5 minutes. Prepared single crystals were placed in glass vials as shown in Fig. 1a. These vials were placed in a stainless-steel pressure vessels lined with a Teflon liner, to which deionized water (18.2 MΩ-cm) was added leaving the vials in a partially submerged state (crystals were not in direct contact with water).

---

[a] *Chemical Science Division, Oak Ridge National Laboratory, Oak Ridge, USA. E-mail: starchenkov@ornl.gov*
[b] *Center for Nanophase Materials Sciences, Oak Ridge National Laboratory, Oak Ridge, USA*

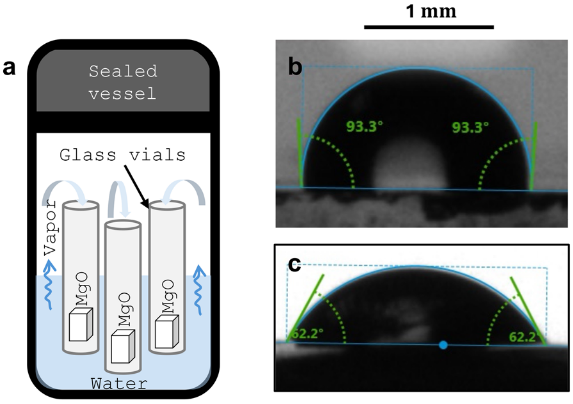

Fig. 1 a) Schematic of the experimental setup for exposing the MgO crystals to water vapor at different temperatures. b) Contact angle measurement on freshly cleaved MgO single crystal. c) Contact angle measurement on MgO exposed to air for 27 years.

After airtight sealing of the pressure vessel, they were kept in furnaces heated to 50 °C and 150 °C for 48 and 96 hours. To minimize the temperature gradient, the pressure vessels were preheated to the target temperature prior to placing them in the furnace. When heated, water vapor generated in the vessel interacts with the MgO crystals in the vials. A representative sample was analyzed using Raman spectroscopy to identify reaction product phase (Fig. S4).

To estimate wettability of the MgO samples a set of contact angle measurements were done at ambient condition using a contact angle goniometer. Experimental details are included in SI. Contact angles measured on freshly cleaved MgO single crystals averaged ~96°. After a few minutes, the contact angle changed to ~89° indicating that a surface reaction occurs. These averages were taken from two experiments, in the first the initial contact angle was 96.7°, and changed to 83.3°. In the second, the starting contact angle was 95.5°, which changed to 94.5° and then 93.3° (Fig. 1b).

For the MgO surfaces exposed to air for 27 years, measured contact angles were 62.2°, 75.7°, 75.6°, 91.5° and 91.8° (Fig. S2 and S3). Thus, several angle values are observed between ~60° and ~90° (Fig. 1c).

Measurements of contact angle on freshly cleaved MgO crystal and the surface exposed to ambient air for 27 years (Fig. 1b and c) were conducted to identify a range of contact angle values assuming after 27 years surface chemistry and wettability reached a steady state. The results indicate that the contact angle in average is smaller for the "aged" surface in comparison to the freshly cleaved. Therefore, the surface becomes more hydrophilic with time. In experiment a freshly cleaved surface was used. Since time between cleaving and the start of the experiment is nonzero, we assume that the contact angle at the beginning of the experiment is slightly lower than the average ~96°, however, never becomes lower than ~60° observed on the 27-year old MgO.

During the hydration experiment we observed the formation of $Mg(OH)_2$ precipitate as identified by Raman spectroscopy (Fig. S4) on the surface of the MgO crystal at different equilibrium temperatures and pressures. The mechanism of $Mg(OH)_2$ formation follows the dissolution–precipitation scenario[18,33] in which, first, the magnesium ion is released into the aqueous environment from the MgO surface and then it precipitates as $Mg(OH)_2$. This process requires the presence of liquid water on the MgO crystal surface. Therefore, we assume that liquid water condensates on the MgO surface when it is exposed to water vapor. Fig. 2 shows scanning electron microscopy (SEM) images of the MgO crystals after they were exposed to water vapor at different temperatures for 48 hours. The images show completely different precipitate textures. At 50 °C the $Mg(OH)_2$ forms hemispherical nodules (Fig. 2a) that are distributed across the surface leaving uncovered areas in between. At 150 °C magnesium hydroxide grows as randomly oriented flakes densely covering the surface (Fig. 2b). For comparison, the images of unreacted MgO surface are shown in Fig. S1a. Additionally, evolution of the nodules and flakes are presented in Fig. S1c and e correspondingly. At 50 °C we observe larger nodules along with new smaller ones which cover the surface (Fig. S1c), whereas at 150 °C flakes grow into a relatively uniform passivation layer (Fig. S1e).

We hypothesize that the change in precipitate morphology is due to a nonuniform distribution of liquid water on the MgO crystal surface. To test how water condenses onto MgO we used a phase-field modeling approach in which the

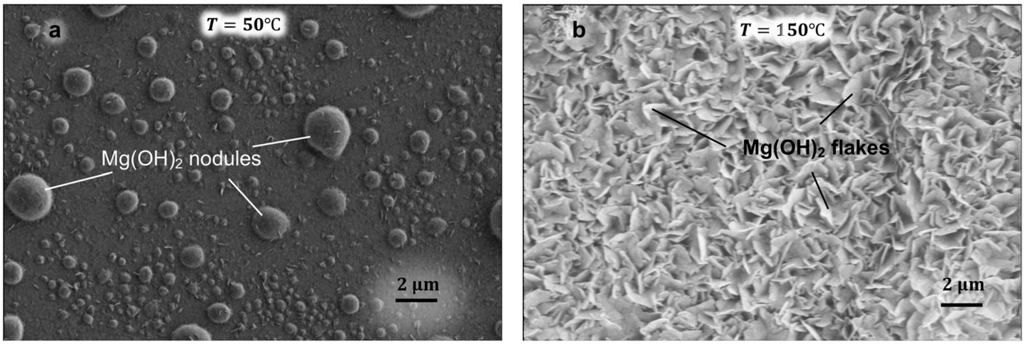

Fig. 2 Scanning electron microscopy (SEM) secondary electron contrast images of hydrated MgO surfaces. a) MgO single crystals reacted at T = 50 °C show separate nodules of reaction products, whereas samples reacted at T = 150 °C (b) show a uniform reaction layer.

liquid–vapor system is simulated as a van der Waals fluid with the vapor–liquid density, ρ, as an order parameter. The generalized Helmholtz free energy consists of a thermodynamic specific free energy, $f_{\mathrm{th}}(\rho)$, and a nonlocal specific free energy, $f_{\mathrm{nl}}(\nabla\rho)$.[29] According to the van der Waals thermodynamic theory of capillarity[34] the homogeneous part of the free energy functional can be expressed as

$$f_{\mathrm{th}} = \frac{\rho RT}{M_{\mathrm{w}}}\ln\frac{c_1\rho}{1-c_1\rho} - c_2\rho, \tag{1}$$

where R – is the gas constant, T is temperature, M_{w} – molar volume of water and $c_1 = \frac{b}{M_{\mathrm{w}}}$ and $c_2 = \frac{a}{M_{\mathrm{w}}}$ are the van der Waals equation of state parameters for water, which include an excluded volume constant, b, and a molecular interaction constant, a. The nonlocal part of the specific free energy is

$$f_{\mathrm{nl}}(\nabla\rho) = \frac{1}{2}T\varepsilon(\nabla\rho)^2, \tag{2}$$

where $\varepsilon = \frac{RT\delta^2}{M_{\mathrm{w}}}\nu$ is related to the thickness of the smooth interface, in which, ν is the specific volume of the liquid phase, and δ is an interface thickness. The parameter δ can be estimated using van der Waals formulation[34] for the surface tension, γ, at the liquid–vapor interface at local equilibrium[28,29]

$$\gamma = \int T\varepsilon(\nabla\rho)^2\mathrm{d}l = \frac{RT\delta}{M_{\mathrm{w}}}\nu(\rho_{\mathrm{l}} - \rho_{\mathrm{v}})^2_{\mathrm{eq}}$$

where $(\rho_{\mathrm{l}} - \rho_{\mathrm{v}})_{\mathrm{eq.}}$ is the difference in liquid and vapor densities at equilibrium.

In this work we assume the conditions to be isothermal. Therefore, the governing equations for the system include mass conservation and momentum conservation (details are in the SI) The chemical potential can be expressed as $\mu = \partial_\rho f_{\mathrm{th}}$, and, since we consider only isothermal conditions, the equation of state, which defines the pressure, P, closes the conservation equations (eqn (S4) and (S5) in SI):

$$P = \rho\mu - f_{\mathrm{th}} \tag{3}$$

To simplify the calculations, we fit eqn (1) using a function that reproduces the shape of the double well potential

$$f^{\mathrm{fit}}_{\mathrm{th}} = C_1(\rho - C_2)^2(\rho - C_3)^2 - C_4\rho \tag{4}$$

where C_1, C_2, C_3, and C_4 are constants. Fig. 3 shows the shape of the homogeneous part of the free energy functional at 50 °C and 150 °C according to eqn (1) and the fit (eqn (4)). To obtain dimensionless free energy density, $\hat{f}$, we scale the eqn (1) with $f_0 = RT_{\mathrm{c}}\rho_{\mathrm{c}}/M_{\mathrm{w}}$, where R is the gas constant, T_{c} – critical temperature for water, ρ_{c} – critical density of water, and M_{w} – molar mass of water. Dimensionless density which represents modeled vapor and liquid water, $\hat{\rho}$, is obtained by scaling with ρ_{c} (scaled quantities are indicated by a hat).

The MgO substrate is modelled as a boundary condition for the density field for water. The Young–Laplace equation, $\cos\theta = \frac{\gamma_{\mathrm{SV}} - \gamma_{\mathrm{LS}}}{\gamma_{\mathrm{LV}}}$, in combination with an expression for the surface tension, provides the boundary condition for density, ρ_{b}, which defines the contact angle between substrate (S), vapor (V), and liquid (L) as:

$$\gamma = \int_{-\infty}^{\infty} T\varepsilon\left(\frac{\partial\rho}{\partial z}\right)^2\mathrm{d}z = \int_{\rho_{\mathrm{V}}}^{\rho_{\mathrm{L}}}\sqrt{2T\varepsilon f_{\mathrm{th}}(\rho)}\mathrm{d}\rho \tag{5}$$

where ρ_{L} is the density of liquid and ρ_{V} is the density of vapor. Following the derivation from Borcia *et al.*[28] the solid surface wettability can be set to model contact angle of 0° at $\rho_{\mathrm{b}} = \rho_{\mathrm{L}}$ and 180° at $\rho_{\mathrm{b}} = \rho_{\mathrm{V}}$. The level of wettability of the MgO surface in the model was described by a contact angle value, which was derived from the Young–Laplace equation and eqn (5).[28] Two temperatures matching the experimental conditions (T = 50 °C and T = 150 °C) were selected to scale the governing equations (eqn (S4) and (S5)) and the equation of state (eqn (1)).

Fig. 4 and 5 show the results of the simulations. Initially, water vapor is distributed across the top of the simulation domain with a constant boundary condition. This provides a vapor supply during the course of the simulation. The MgO surface at the bottom of the simulation domain is defined by the constant boundary density, ρ_{b}, which defines the contact angle (wettability) of the interface. Measurements of the contact angle (Fig. 1b and c) provided a range of contact angles characteristic to the MgO surface. However, these contact angles were measured at ambient conditions, and

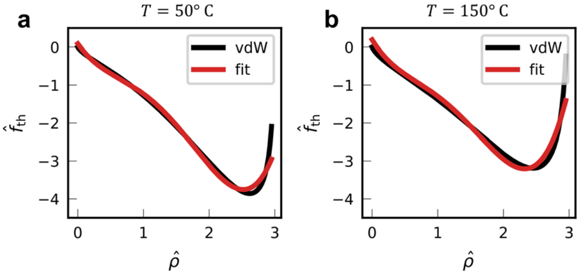

Fig. 3 Normalized free energy density according to the van der Waals thermodynamic theory as a function of normalized water density, $\hat{\rho}$. Black curve is the free energy density obtained from the eqn (1); red curve is a fit using eqn (4). a) Temperature T = 50 °C b) T = 150 °C.

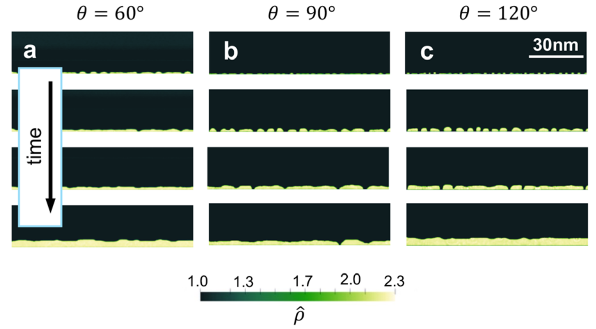

Fig. 4 Phase field modeling results showing the evolution of vapor–liquid density, $\hat{\rho}$, above the substrate at T = 50 °C at different values for contact angle. a) θ = 60° b) θ = 90° c) θ = 120°.

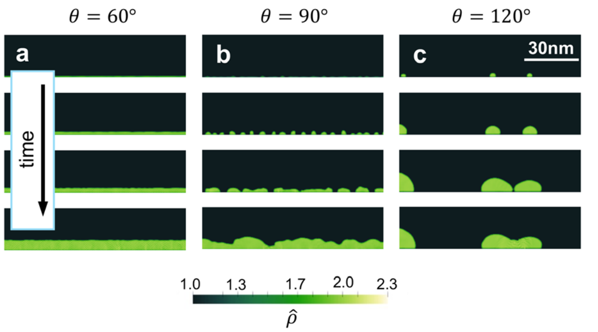

Fig. 5 Evolution of vapor–liquid density, $\hat{\rho}$, above the substrate at T = 150 °C and different values for contact angle a) θ = 60° b) θ = 90° c) θ = 120°.

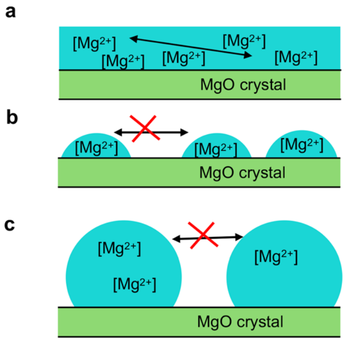

Fig. 6 Schematic of [Mg^{2+}] migration pathways in adsorbed water on the MgO surface before precipitation. a) Uniform water film; b) separate small uniform droplets; c) separate large droplets. Arrows demonstrate ability of magnesium ion, [Mg^{2+}], to travel across the whole surface or being localized within an isolated droplet island.

were likely different during the experiment. In literature a molecular dynamics study indicates that at higher temperatures MgO surface becomes more hydrophilic.[31] Therefore, in simulations we picked three characteristic surface contact angle values which represent varied hydrophobicity: θ = 60° (hydrophilic conditions), θ = 90° (intermediate wetting conditions), and θ = 120° (hydrophobic conditions).

Fig. 4 demonstrates the time evolution of density at different wettability values at 50 °C. For the hydrophilic case (θ = 60°, Fig. 4a) water forms a uniform film the thickness of which increases with time. At θ = 90° water nucleates as small droplets that grow and eventually merge into a film (Fig. 4b). Similar behavior is observed for simulations at θ = 120° (Fig. 4c) as well as at T = 150 °C (Fig. 5). A uniform film is formed at hydrophilic condition (Fig. 5a). However, at θ = 90° and θ = 120° the distribution of densities near the interface is different. At intermediate wettability (θ = 90°) the nuclei start to grow and eventually merge into a film (Fig. 5b). However, the shape of the film surface is irregular in comparison to a lower temperature result (Fig. 4b). At θ = 120° a smaller number of nuclei droplets form. These grow without creating additional nuclei. This results in smaller number of larger droplets on the surface (Fig. 5c).

Discussion

During hydroxylation of MgO magnesium ions are initially dissolved in liquid water which allows migration of dissolved ions and later precipitation when the local concentration reaches saturation. This mechanism requires liquid water to be present at the MgO surface to trigger dissolution. Observation of precipitate structures, which depend on the temperature of the experiment, provides information on the distribution of $Mg(OH)_2$ and, therefore, water, on the surface of the initial MgO crystal (Fig. 2). The main observed difference between the experiments is that at T = 50 °C the precipitate is distributed nonuniformly across the MgO crystal surface whereas at T = 150 °C flaky a precipitate uniformly covers the surface. The rates of dissolution and precipitation are also likely different, which might explain the shape of the precipitating crystalline solids. However, the fact that the precipitate at T = 50 °C forms polycrystalline nodules and not isolated single crystals with well-defined crystallographic surfaces shows that the nonuniform distribution of $Mg(OH)_2$ on the surface cannot only be explained by slower reaction rates. It must reflect limited magnesium ion transport that confines the precipitate to the regions of the hemispheres. Therefore, the primary transport limiting mechanism is the non-uniform distribution of water, which forms isolated islands which surface tension forces into droplets. As a result, magnesium ion transport is far less limited when the surface is covered by a homogeneous water film (Fig. 6a) and is significantly limited when water is distributed as isolated islands (droplets) as shown in Fig. 6b and c.

Simulation results demonstrate that temperature doesn't have a qualitative effect on the distribution of water on the MgO surface (uniform film does not become droplets). However, increased temperature amplifies the effect of substrate wettability on the distribution of water droplets. Computationally, the largest droplets are formed under hydrophobic condition at higher temperature (Fig. 5c). This, however, contradicts the experimental observations (Fig. 1b). This suggests that the surface properties of the MgO change at higher temperatures, which is consistent with a molecular dynamics study of the surface.[31] Thus, our study reveals that the shape and distribution of the precipitate is likely a result of the distribution of liquid water on the surface of MgO during a dissolution–precipitation reaction. Moreover, surface wettability plays a key role in whether the reaction occurs in a homogeneous water film or in isolated droplets.

Overall, the molecular dynamics simulation study[31] reports on the reduction of the MgO–water contact angle as temperature rises, which is linked to decrease in the density of hydrogen bonds. Our phase filed simulation results demonstrate weak dependency of water distribution near the surface on shape equation of state at 50 °C and 150 °C, however, strong dependency on wetting (contact angle). Since in experiment we observed isolated nodules at lower temperature and crystals uniformly distributed over the surface at higher temperature, we conclude the correlation between those structures and substrate wettability.

In summary, we observed the formation of $Mg(OH)_2$ precipitates on the MgO crystal surface where reaction in vapor led to dissolution–precipitation reactions. Experiments at T = 50 °C and T = 150 °C yielded different precipitate textures: uniformly distributed flaky structures *versus* nonuniformly distributed droplet-like shapes. Phase field modelling demonstrated that this was controlled by the wettability of the surface, and suggested that temperature amplifies the transition from hydrophilic to hydrophobic behaviour. On wettable surfaces water condenses as a liquid film, whereas on non-wettable surfaces water nucleates as small droplets. Comparing the experimental and simulation results we conclude that temperature changes the surface properties of MgO which results in switching between the spatially limited to unlimited transport of ions at the MgO interface.

Conflicts of interest

There are no conflicts to declare.

Data availability

All additional experimental data are presented in the supplementary information (SI).

All details of the model and simulation parameters are presented in the SI.

Additionally, the scripts to run simulation can be found in Mendeley Data repository: Starchenko, Vitalii; Adapa, Sai; Anovitz, Lawrence; Ivanov, Ilia; Stack, Andrew; Yuan, Ke; Weber, Juliane (2026), “Data associated with "Role of Liquid Water Distribution in MgO Hydroxylation"”, Mendeley Data, V1, DOI: https://10.17632/yzxpvtd2dp.1, https://data.mendeley.com/datasets/yzxpvtd2dp/1

Supplementary information is available. See DOI: https://doi.org/10.1039/d6ce00207b.

Acknowledgements

This work was supported by the U.S. Department of Energy, Office of Science, Basic Energy Sciences (BES), Materials Sciences and Engineering Division. This research used resources of the Compute and Data Environment for Science (CADES) at the Oak Ridge National Laboratory, which is supported by the Office of Science of the U.S. Department of Energy under Contract No. DE-AC05-00OR22725. Contact angle measurements and SEM characterization was conducted at the Center for Nanophase Materials Sciences, which is a DOE Office of Science User Facility. Andrew Miskoviec is acknowledged for access to the Raman instrument. Portions of this work (Raman characterization) were generated using instrumentation supported by the National Nuclear Security Administration.

References

1 I. Spasojevic, A. Verdaguer, G. Catalan and N. Domingo, *Adv. Electron. Mater.*, 2022, **8**, 2100650.
2 H. Zhang, Y. Shen, P. Sharma, L. Wang, D. Zhang, K. Ooe, S. Kobayashi, Y. Shimakawa, D. Kan and J. Seidel, *Mater. Horiz.*, 2025, **12**, 5762–5770.
3 F. Berg, N. Kopperberg, J. Lübben, I. Valov, X. Wu, U. Simon and U. Böttger, *J. Appl. Phys.*, 2023, **134**, 185106.
4 T. H. Buyuklimanli and J. H. Simmons, *Phys. Rev. B: Condens. Matter*, 1991, **44**, 727–733.
5 B. P. Kore, M. Jamshidi and J. M. Gardner, *Mater. Adv.*, 2024, **5**, 2200–2217.
6 F. Baumann, S. R. Raga and M. Lira-Cantú, *APL Energy*, 2023, **1**(1), 011501.
7 J. Weber, B. Moseley, K. Yuan, B. R. Evans, V. Starchenko, E. T. Rodriguez, D. Y. Chung, M. G. Boebinger, M. A. Mcguire, G. Yumnam, R. P. Hermann, L. M. Anovitz and A. G. Stack, *J. Phys. Chem. C*, 2024, **129**, 194–204.
8 J. Weber, V. Starchenko, K. Yuan, L. M. Anovitz, A. V. Ievlev, R. R. Unocic, A. Y. Borisevich, M. G. Boebinger and A. G. Stack, *Environ. Sci. Technol.*, 2023, **57**, 14929–14937.
9 Y. Zhang, Y. S. Gao, H. Pfeiffer, B. Louis, L. Y. Sun, D. O'Hare and Q. Wang, *J. Mater. Chem. A*, 2019, **7**, 7962–8005.
10 M. Brahlek, A. S. Gupta, J. Lapano, J. Roth, H. T. Zhang, L. Zhang, R. Haislmaier and R. Engel-Herbert, *Adv. Funct. Mater.*, 2018, **28**, 1702772.
11 Y. Sharma, M. C. Lee, K. C. Pitike, K. K. Mishra, Q. Zheng, X. Gao, B. L. Musico, A. R. Mazza, R. S. Katiyar, V. Keppens, M. Brahlek, D. A. Yarotski, R. P. Prasankumar, A. Chen, V. R. Cooper and T. Z. Ward, *ACS Appl. Mater. Interfaces*, 2022, **14**, 11962–11970.
12 Y. Sharma, A. R. Mazza, B. L. Musico, E. Skoropata, R. Nepal, R. Jin, A. V. Ievlev, L. Collins, Z. Gai, A. Chen, M. Brahlek, V. Keppens and T. Z. Ward, *ACS Appl. Mater. Interfaces*, 2021, **13**, 17971–17977.
13 W. Zhang, A. R. Mazza, E. Skoropata, D. Mukherjee, B. Musico, J. Zhang, V. M. Keppens, L. Zhang, K. Kisslinger, E. Stavitski, M. Brahlek, J. W. Freeland, P. Lu and T. Z. Ward, *ACS Nano*, 2020, **14**, 13030–13037.
14 P. Yang, J. N. Bracco, G. Camacho Meneses, K. Yuan, J. E. Stubbs, M. D. Boamah, M. Brahlek, M. Sassi, P. J. Eng, M. G. Boebinger, A. Borisevich, A. K. Wanhala, Z. Wang, K. M. Rosso, A. G. Stack and J. Weber, *Environ. Sci. Technol.*, 2025, **59**, 3484–3494.
15 N. McQueen, P. Kelemen, G. Dipple, P. Renforth and J. Wilcox, *Nat. Commun.*, 2020, **11**, 1–10.
16 X. X. Zhang, K. P. Qiu, E. Levänen and Z. X. Guo, *CrystEngComm*, 2014, **16**, 8825–8831.
17 M. Sassi and K. M. Rosso, *Phys. Chem. Chem. Phys.*, 2024, **26**, 2269–2276.
18 S. Adapa, K. Yuan, B. R. Evans, J. Weber, S. Irle, L. M. Anovitz and A. G. Stack, *J. Mater. Chem. A*, 2025, **13**, 27367–27376.
19 A. Kondo, R. Kurosawa, J. Ryu, M. Matsuoka and M. Takeuchi, *J. Phys. Chem. C*, 2021, **125**, 10937–10947.

20 M. Pettauer, A. Baldermann, S. Eder and M. Dietzel, *Cryst. Growth Des.*, 2024, **24**, 3085–3092.

21 A. Raponi, S. Romano, G. Battaglia, A. Buffo, M. Vanni, A. Cipollina and D. Marchisio, *Cryst. Growth Des.*, 2023, **23**, 4748–4759.

22 L. Dostie, K. Rausis and I. M. Power, *J. Cleaner Prod.*, 2024, **457**, 142394.

23 M. M. Paulsen, S. G. R. Nielsen, F. J. Tilsted and T. H. Pedersen, *J. CO2 Util.*, 2025, **102**, 103255.

24 K. Rausis, A. R. Stubbs, I. M. Power and C. Paulo, *Int. J. Greenhouse Gas Control*, 2022, **119**, 103701.

25 Q. R. S. Miller and H. T. Schaef, *Environ. Sci.: Adv.*, 2022, **1**, 426–429.

26 Q. R. S. Miller, J. P. Kaszuba, S. N. Kerisit, H. T. Schaef, M. E. Bowden, B. P. McGrail and K. M. Rosso, *Environ. Sci.: Nano*, 2020, **7**, 1068–1081.

27 N. T. Luong, N. Veyret and J. F. Boily, *ACS Appl. Mater. Interfaces*, 2023, **15**, 45055–45063.

28 R. Borcia, I. D. Borcia and M. Bestehorn, *Phys. Rev. E:Stat., Nonlinear, Soft Matter Phys.*, 2008, **78**, 066307.

29 A. G. Lamorgese and R. Mauri, *Phys. Fluids*, 2009, **21**, 044107.

30 D. Wheeler, J. A. Warren and W. J. Boettinger, *Phys. Rev. E: Stat., Nonlinear, Soft Matter Phys.*, 2010, **82**, 051601.

31 C. Zhang, X. Li and J. S. Wang, *J. Phys. Chem. C*, 2019, **123**, 18914–18923.

32 M. M. Abraham, C. T. Butler and Y. Chen, *J. Chem. Phys.*, 1971, **55**, 3752–3756.

33 S. Bonilla-Correa, C. Ruiz-Agudo, P. Alvarez-Lloret, Y. Emminger, C. Rodriguez-Navarro and E. Ruiz-Agudo, *Contrib. Mineral. Petrol.*, 2025, **180**, 87.

34 J. S. Rowlinson, *J. Stat. Phys.*, 1979, **20**, 197–200.